

Ferroelectricity Modulates Polaronic Coupling at Multiferroic Interfaces

Marius-Adrian Husanu (✉ ahusanu@infim.ro)

National Institute of Materials Physics <https://orcid.org/0000-0003-4510-6653>

Dana Popescu

National Institute of Materials Physics

Luminita Hrib

National Institute of Materials Physics

Raluca Negrea

National Institute of Materials Physics

Cosmin Istrate

National Institute of Materials Physics

Lucian Pintilie

National Institute of Materials Physics

Cristian Teodorescu

National Institute of Materials Physics

Federico Bisti

Leonid Lev

Moscow Institute of Physics and Technology

Andrey Mishchenko

RIKEN Center for Emergent Matter Science (CEMS)

Thorsten Schmitt

Paul Scherrer Institut <https://orcid.org/0000-0002-5737-1094>

Iuliana Pasuk

National Institute of Materials Physics

Lucian Filip

National Institute of Materials Physics <https://orcid.org/0000-0001-7319-1758>

Vladimir Strocov

Paul Scherrer Institute <https://orcid.org/0000-0002-1147-8486>

Article

Keywords: multiferroics, electron-phonon interaction, angle resolved photoelectron spectroscopy, interface engineering

Posted Date: January 14th, 2022

DOI: <https://doi.org/10.21203/rs.3.rs-1208929/v1>

License:  This work is licensed under a Creative Commons Attribution 4.0 International License.

[Read Full License](#)

Version of Record: A version of this preprint was published at Communications Physics on August 15th, 2022. See the published version at <https://doi.org/10.1038/s42005-022-00983-3>.

Ferroelectricity modulates polaronic coupling at multiferroic interfaces

Marius Adrian Husanu^{1,2}, Dana Georgeta Popescu², Federico Bisti^{1,3}, Luminita Mirela Hrib², Lucian Dragos Filip², Iuliana Pasuk², Raluca Negrea², Cosmin Istrate², Leonid Lev^{1,4}, Thorsten Schmitt¹, Lucian Pintilie², Andrey Mishchenko⁵, Cristian Mihail Teodorescu² and Vladimir N. Strocov¹⁺*

¹ Swiss Light Source, Pauls Scherrer Institute, 5232 Villigen-PSI, Switzerland

² National Institute of Materials Physics, Atomistilor 405A, 077125 Magurele, Romania

³ CELLS-ALBA Synchrotron Radiation Facility, Carrer de la Llum 2-26, 08290 Cerdanyola del Valles, Barcelona, Spain

⁴ Moscow Institute of Physics and Technology, 141700 Dolgoprudny, Russia

⁵ RIKEN Center for Emergent Matter Science (CEMS), 2-1 Hirosawa, Wako, 351-0198, Saitama, Japan

Email:

* ahusanu@infim.ro

+vladimir.strocov@psi.ch

Keywords: multiferroics, electron-phonon interaction, angle resolved photoelectron spectroscopy, interface engineering

Abstract

Physics of the multiferroic interfaces is currently understood mostly within a phenomenological framework including screening of the polarization field and depolarizing charges. Largely unexplored still remains the band dependence of the interfacial charge modulation, as well as the associated changes of the electron-phonon interaction, coupling the charge and lattice degrees of freedom.

Here, multiferroic heterostructures of the colossal-magnetoresistance manganite $\text{La}_{1-x}\text{Sr}_x\text{MnO}_3$ buried under ferroelectric BaTiO_3 and $\text{PbZr}_x\text{Ti}_{1-x}\text{O}_3$ are explored using soft-X-ray angle-resolved photoemission. The experimental band dispersions from the buried $\text{La}_{1-x}\text{Sr}_x\text{MnO}_3$ identify coexisting two-dimensional hole and three-dimensional electron charge carriers. The ferroelectric polarization modulates their charge density, changing the band filling and orbital occupation in the interfacial region. Furthermore, these changes in the carrier density affect the coupling of the 2D holes and 3D electrons with the lattice which forms large Froelich polarons inherently reducing mobility of the charge carriers. We find that the fast dynamic response of electrons makes them much more efficient in screening of the electron-lattice interaction compared to the holes. Our k -resolved results on the orbital occupancy, band filling and electron-lattice interaction in multiferroic oxide heterostructures modulated by the ferroelectric polarization disclose most fundamental physics of these systems needed for further progress of *beyond-CMOS* ferro-functional electronics.

Introduction

The proximity of the hole-doped manganite $\text{La}_{0.7}\text{Sr}_{0.3}\text{MnO}_3$ (LSMO) and a FE material with a well-defined orientation of the FE polarization (\mathbf{P}), provides a local tuning of the doping level close to the interface^{1,2}. Charge modulation in the interfacial region of LSMO occurs in order to compensate the unscreened depolarizing field due to the discontinuity in the ferroelectric

polarization^{3–5}, with its spatial localization related to the Thomas-Fermi screening length⁶. An electrostatic picture of compensating the FE polarization assumes a charge depletion in LSMO when \mathbf{P} points towards the interface, and a charge accumulation when it points in the opposite direction^{2,7,8}. However, the final picture of the interface-altered electronic structure extends beyond electrostatic-derived arguments. On one hand, the Schottky barrier height between the two joining materials and the FE state control the band alignment and band bending at the interface, and thus the transfer of electrons and holes accounting for compensation of the FE phase^{3,4,9,10}. Then, the orbital and lattice degrees of freedom (DOF) come into play when strain^{11,12} in conjunction with ferroelectric-like distortions⁵ and octahedral tilts,¹³ propagating into the interfacial region, modulate the Mn-O bond lengths as compared to the bulk. By lifting orbital degeneracy, it changes the orbital-dependent charge occupations and itinerancy of the carriers^{7,8,14}.

The coupling between the charge and lattice DOFs expresses the polaronic nature of the propagating electron/hole, dressed by the local lattice distortion in the form of a phonon cloud. Such coupled charge-lattice quasiparticles explain the superconductive pairing mechanism¹⁵, the transition from high to low mobility in colossal magnetoresistance materials¹ and the strong charge localization close to the metal-to-insulator transition in Mott insulators^{16,17}. Hence, understanding how electron-phonon interaction (EPI) renormalizes the electron and hole effective mass (m_{eff}) and therefore their mobility is essential for pushing forward oxide electronics beyond the known paradigms. However, addressing the impact of EPI on the interface electronic structure is experimentally challenging since most spectroscopic techniques, by probing the whole heterostructure depth, can rarely isolate the contribution of the contact region only. One way of extracting such information is from the spectral function, $A(\mathbf{k},\omega)$ ¹⁸ which contains the effect of all many-body (electron-electron and electron-boson) interactions. It is directly accessed by angle-resolved photoelectron spectroscopy (ARPES), with the EPI signature being a dip-hump structure of $A(\mathbf{k},\omega)$ accompanying the quasiparticle peak (QP) at low band filling and kinks in the experimental band dispersion^{18,19} at large occupations of the conduction band. Our study uses soft X-ray ARPES^{20,21}, whose probing depth matches the interfacial region and whose sharp intrinsic resolution in the out-of-plane momentum k_z allows precise sampling of the 3D \mathbf{k} -space, to access electronic properties of the LSMO interface buried under thin FE layers of BaTiO₃ (BTO) and PbZr_{0.2}Ti_{0.8}O₃ (PZT), which propagate the

hole-depletion state into the joining LSMO region. We reveal aspects which so far remained hidden due to either the extreme surface sensitivity and consequently large k_z broadening²⁰ of conventional ultra-violet ARPES, or the angle-integrated nature of the transport measurements¹⁴, X-ray photoelectron spectroscopy^{4,10,4,10} and X-ray absorption spectroscopies^{1,2,7,14}, previously used to probe such interfaces.

Our results establish the coexistence of hole-coupled 2D and electron-coupled 3D Fröhlich polarons (FP) in LSMO. We show that the polaronic-coupling strength can be tuned by the FE polarization through the preferential occupation of the $e_g(3z^2-r^2)$ orbitals vs $e_g(x^2-y^2)$ ones. Such altered orbital occupation modifies in turn the relative electron/hole density and changes their contribution at the screening of the electron-phonon coupling. In addition, we resolve the subtle balance between hole depletion and electron accumulation which stabilize the well-defined polarization state of the FE top layer in multiferroic heterostructures.

Results and Discussion

The essential aspect of our experiments is the preparation of multiferroic heterostructures, where the FE layer is thin enough to access the electronic structure of the buried interface with soft X-ray photoemission, and in the same time stays above the critical thickness of $\sim 3\text{-}6$ unit cells at which PZT and BTO lose their FE character^{5,22}. Such thin FE films, epitaxially grown and strained at the in-plane lattice constant of the substrate, stabilize as a single FE domain due to their high coercive field. \mathbf{P} pointing either towards (\mathbf{P}^-) or away from the interface (\mathbf{P}^+)⁵ are opposed by corresponding depolarizing field, compensated by the modulation of the LSMO charge carriers. Other possible extrinsic mechanisms such as such as adsorption of polar molecules at the FE surfaces may also have a contribution in stabilizing the ferroelectric state^{23,24}. For details on the FE state of the top layers see Section 1 and Fig. S1 from Supplementary Material (SM).

The high coercive field of the 3 nm-thin FE layers means that *in-situ* switching of the ferroelectric state between two opposed states $\mathbf{P}^-/\mathbf{P}^+$ is excluded. We will focus instead on comparing the signature of the bare LSMO surface, unmodified by the proximity effect of FEs with the \mathbf{P}^- interface which is stabilized by the LSMO substrate. We will follow the gradual

evolution of charge density and orbital order induced at the interface by ferroelectrics with different magnitude of \mathbf{P} ; with $\mathbf{P}_{\text{BTO}} \sim 20 - 30 \mu\text{C}/\text{cm}^3$ and $\mathbf{P}_{\text{PZT}} \sim 60 - 80 \mu\text{C}/\text{cm}^{25,23}$.

Different occupation probabilities of the otherwise degenerated e_g orbitals in half-filled LSMO result from a competition between the substrate-induced strain and breaking of the symmetry at the surface and interface^{11,12}. The strain lowers the crystal symmetry²⁵, and Jahn-Teller octahedral rotations lift the orbital degeneracy^{8,25}. In-plane tensile strain ($c/a < 1$) lowers the energy of the $e_g(x^2-y^2)$ orbitals, increasing their occupation probability, while compressive strain ($c/a > 1$) lowers the energy and increases occupation of the $e_g(3z^2-r^2)$ ones⁸. These effects alter hopping probabilities between Mn orbitals with the in-plane and out-of-plane symmetries. On the other hand, breaking of symmetry near the surface always favors the $e_g(3z^2-r^2)$ occupation^{11,12}. Joining strained LSMO and epitaxially grown FE oxides further modulates the orbital occupation such that \mathbf{P}^- , oriented towards the LSMO contact, increases the $e_g(3z^2-r^2)$ occupation, while the opposite \mathbf{P}^+ direction enhances the $e_g(x^2-y^2)$ occupation^{7,8}.

Electron microscopy images with atomic and chemical resolution in Fig. 1A reveal mostly the LaSrO|TiO₂ transition sequence from LSMO to PZT, with some intermixing limited at the first interface layer (see *MM*). Details on the signatures of the substrate strain in X-ray diffraction and microscopy images of the BTO|LSMO interface are in Fig. S2. Hence, our LSMO/FE interfaces prepared mostly in the LaSrO|TiO₂ sequence, minimise the e_g splitting Δe_g between the $3z^2-r^2$ and x^2-y^2 orbitals¹² due to competing strain and termination effects, while \mathbf{P} oriented towards LSMO to increase occupation of the $e_g(3z^2-r^2)$ states^{7,8}. For details on growth methodology see *Materials and Methods (MM)* and SM 2.

First-principles density-functional-theory (DFT) calculations on LSMO, strained to the in-plane STO lattice constant, are represented in Fig. 1B. They indicate a coexistence of two types of charge carriers at the Fermi level E_F : light electrons ($m_{\text{eff}} \sim 0.4 m_e$, where m_e is the free-electron mass of the electron) in the $e_g(3z^2-r^2)$ derived 3D bands, and heavier holes ($m_{\text{eff}} \sim 1.4$) in the quasi-2D $e_g(x^2-y^2)$ derived bands, which are degenerate in the Γ point. The corresponding Fermi surface (FS), represented in Fig. 1C is qualitatively similar with previous works and experimental results^{26,27}. It features the 3D electron pocket around Γ , with only a slight mass anisotropy along the ΓM and ΓX directions, having the $e_g(3z^2-r^2)$ with an admixture of $e_g(x^2-y^2)$.

The heavy quasi-2D holes define the FS pocket around the R point, with carriers having predominantly the $e_g(x^2-y^2)$ character²⁶. The experimental in-plane FS maps recorded at two photon energies $h\nu$ near the Γ X_M and X_ZAR planes of the Brillouin zone (BZ) are represented in Fig. 1(D,F) for bare LSMO and in Fig. 1(E,G) for the LSMO|BTO heterostructure. Superimposed on the experimental FSs are the calculated FS of the strained LSMO. The out-of-plane FS map in Fig. 1H identifies the 3D character of the interface electrons. The Luttinger volume²⁸ of the electron and hole pockets, represented by their areas in the experimental FS cuts, quantifies the corresponding concentrations of electrons (n_e) and holes (n_h). For additional analysis of the ARPES data see Section 4 of the SM. Having established the \mathbf{k} -space structure of the electron and hole states, we will now explore the impact of the FE-induced charge density modulation on the concentration and polaronic effective-mass renormalization of the electrons and holes.

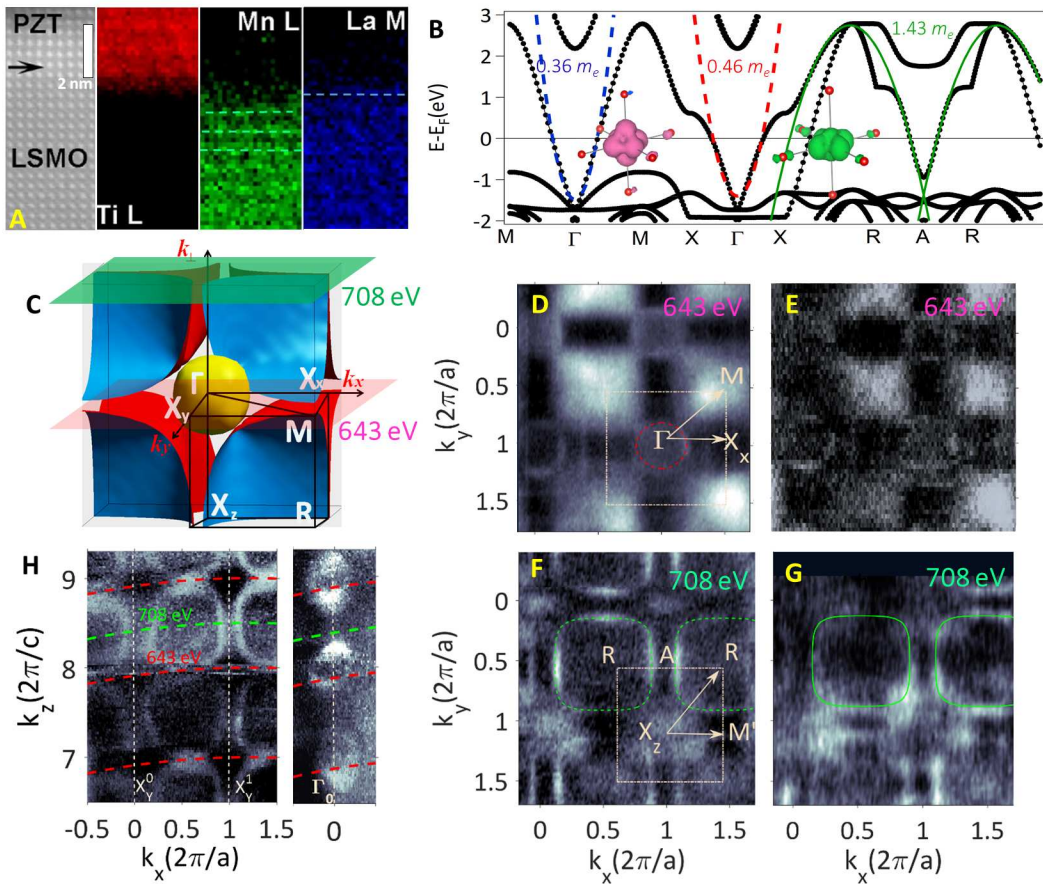


Figure 1. Structural and electronic properties. (A) High resolution HAADF-STEM image at PZT-LSMO interface, and Ti L, Mn L and La M maps at atomic level. The RGB map (right panel) was obtained by overlapping the Ti, Mn and La maps. (B) Theoretical DFT+U band structure for STO-strained pseudocubic LSMO and (insets) local density of states integrated ± 0.2 eV around the Γ and A bands bottom. (C) Calculated Fermi surface (FS) for strained LSMO. (D,F) In-plane FS maps for bare LSMO in the Γ MX and X_Z AR planes recorded with $h\nu=643$ eV and 708 eV, respectively. (E,G) The corresponding FS maps of the LSMO|BTO heterostructure, showing an increase of the electron concentration n_e and decrease of the hole one n_h . (H) Experimental out-of-plane FS maps for the LSMO|BTO heterostructure in the X_Y MR and $\Gamma X_x M'$ planes

FE-induced charge density modulation

First, we will analyze the FE-induced modulation of the charge density represented by the ARPES data. The images in Fig. 2A, B, recorded with 708 eV, represent band dispersions within the cube-like hole pocket along the RAR direction of the BZ for bare LSMO (A) and for the PZT|LSMO interfaces (B). Superimposed on top are the fits of the momentum distribution curves (MDC) maxima through the binding energies (traced by blue dots); the MDCs at E_F (yellow line) whose gradient indicates the Fermi momentum k_F . ARPES images of the BTO|LSMO system recorded in the same conditions are in Fig. S4. Table 1 reports the hole densities, calculated using the Luttinger formula from the experimental k_F values as

$$n_h = \left(2\pi/a - 2k_F\right)^3 / (2\pi)^3 \quad (1)$$

assuming approximately cubic shape of hole pockets. These results demonstrate that the FE polarization significantly depletes n_h at the LSMO|FE interfaces compared to bare LSMO surface. The gradual decrease of n_h manifests the expected hole-depletion state, induced in the LSMO substrate by the \mathbf{P}^+ state of the FE top layer, where the FE field is compensated by carriers from LSMO^{2,4}. This evolution directly measures the increasing value of \mathbf{P} in BTO and PZT.

The microscopic mechanism of interface coupling is a combined effect of:

1. charge building up in LSMO close to the interface with the FE in order to compensate the bound FE charges and the resulting depolarizing field, stabilizing the well-defined orientation of \mathbf{P}^9 . This charge depends on both the magnitude of \mathbf{P} and on the amount of intrinsic compensation charges already available in the FE through self-doping mechanisms²³. For the same layer

thickness ~ 3 nm, the density of free carriers in BTO, with its oxygen vacancy-assisted n-type conduction, exceeds by at least one order of magnitude that of PZT³. Hence, it requires less compensation charges in the metallic electrode to stabilize the inwards \mathbf{P}^- state. Accordingly, the alteration of the LSMO electronic structure expressed by the experimental n_h values is weaker when interfacing to BTO than to PZT³.

2. FE instability, consisting in off-centering of the cations, modified tetragonality and octahedral tilts in the top layer which propagates into LSMO within the first unit cells, lowering energy of the e_g orbitals and favoring their preferential occupation⁶⁻⁸. This effect has also been shown to directly scale with the magnitude of \mathbf{P} through the cation displacement with respect to the centro-symmetric configuration, propagating into LSMO. Such instability induced by the PZT layer^{23,29} is at least by a factor of two larger compared to BTO¹⁴. Consequently, its impact on the electronic structure through the induced displacement of the Mn atoms from the central position, modified tetragonality ratio (c/a) and octahedral conformation is also stronger^{5,8,13}.

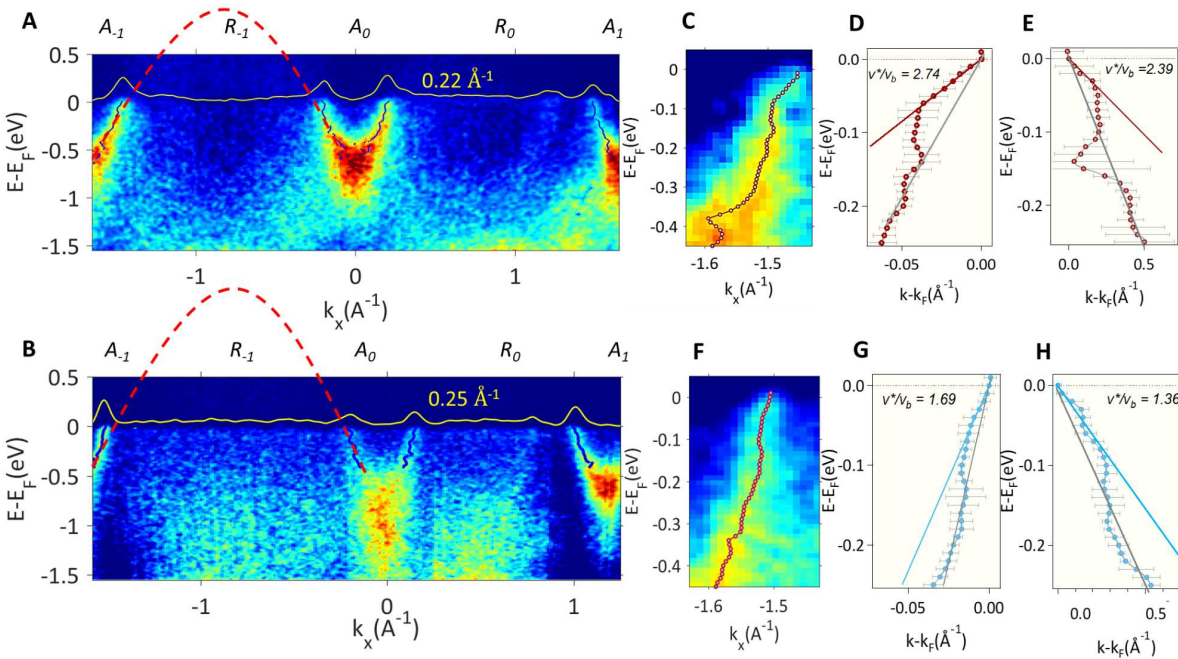


Figure 2. Quasi-2D hole bands and dispersion kinks. (A,B) ARPES images recorded at $h\nu=708$ eV and p -polarized light along the RAR direction, probing the hole bands for LSMO surface (A), and for LSMO|PZT (B) interfaces. The dots superimposed on each image are the MDC maxima, with the MDCs at E_F (yellow lines) used to extract k_F

values. The dashed lines are guide for the eyes indicating the hole band. (**C, F**) Zoom into the low-energy region of the experimental bandstructure around A_{-1} point for LSMO bare surface (**C**) and LSMO|PZT interface (**F**). The superimposed dots are the MDC maxima which identifies the kinks in the parabolic dispersion of the hole bands. (**D, E, G, H**) MDC maxima and their linear fits corresponding to the bare and renormalized dispersions in the kink region for LSMO surface (**D,E**), and for LSMO|PZT (**G,H**) interfaces around two different points of the BZ: A_{-1} (**D,G**) and A_1 (**E,H**).

		LSMO	LSMO BTO	LSMO PZT
k_F (\AA^{-1})	hole band	0.22 ± 0.08	0.23 ± 0.11	0.25 ± 0.10
	electron band	0.30 ± 0.05	0.35 ± 0.08	0.36 ± 0.07
n (cm^3)	hole band	6.42×10^{21}	6.18×10^{21}	5.65×10^{21}
	electron band	0.46×10^{21}	0.75×10^{21}	0.82×10^{21}

Table 1 Modulation of carrier concentrations. Experimental Fermi wavevectors extracted from MDCs at E_F for the bands defining the hole and electron pockets, and the corresponding hole and electron densities for LSMO in comparison with the LSMO|FE interfaces.

For the electron states, the effect of the FE polarization is clear from the ARPES data in Figure 3. The latter compares the ARPES images for the LSMO|PZT interface and bare LSMO recorded at the Mn $2p$ resonance in the ΓX direction. These images represent band dispersions for the $e_g(3z^2-r^2)$ derived electron pockets centered at the Γ point (Fig. 1 D-F) through two BZs. The experimental k_F values and the corresponding electron densities, evaluated assuming approximately spherical shape of electron pockets and also presented in Table 1, and show the increase when going from LSMO to the buried LSMO|PZT interface (D). The ARPES images for the LSMO|BTO interface are shown in Figs. S6 in Section 3.2 from SM. Therefore, the FE polarization oriented inwards (**P**) results indeed in accumulation of additional electrons in the interfacial region of the LSMO|FE heterostructures compared to the LSMO surface, in agreement with previous experiments^{2,7}. However, our measurements allow for the first time a distinct

separation of the electron and hole contribution to the total FE-induced charge density $n=n_h-n_e$. We will see below that although n_e is significantly smaller than n_h , its increase predominates in screening of EPI and corresponding renormalization of the charge carrier's m_{eff} .

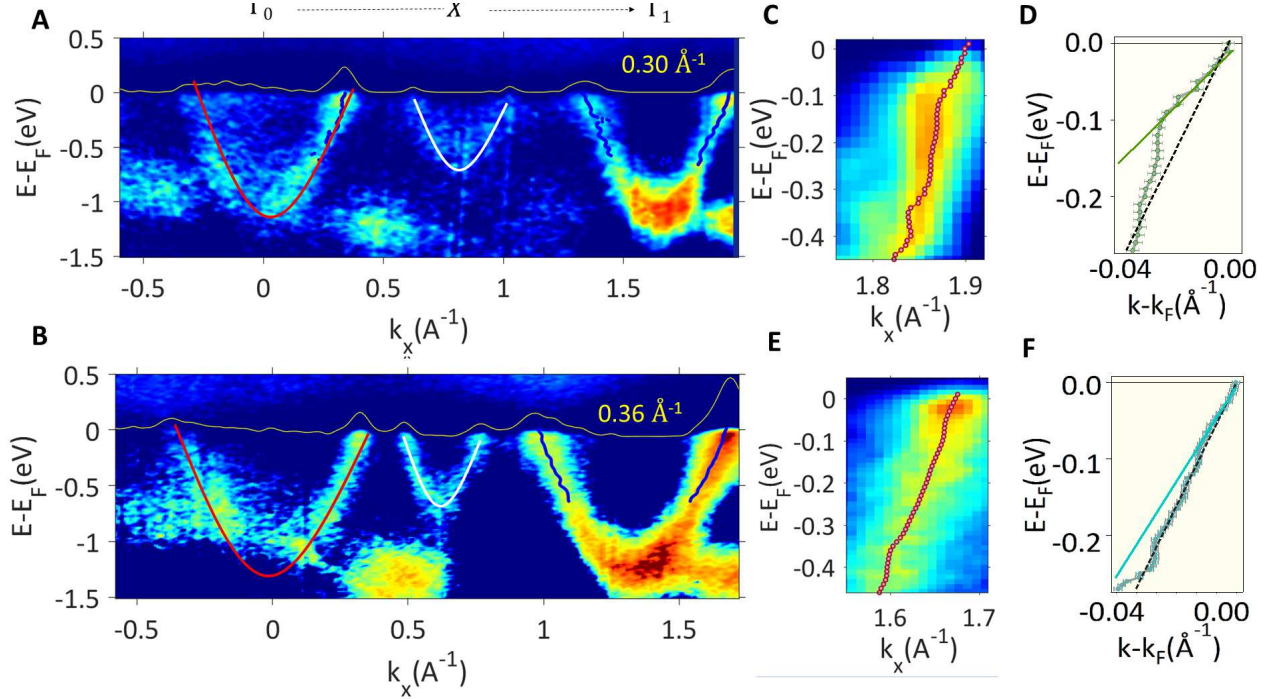


Figure 3. 3D electron bands and dispersion kinks. ARPES images recorded with $h\nu=643$ eV and p -polarized light along the ΓX direction, probing the electron bands for LSMO (A) and LSMO|PZT interface (B). The MDCs at E_F (yellow lines) are used to extract the k_F values. The superimposed lines are guides for the eye showing the parabolic dispersion. (C,E) Zoom-in of the ARPES images in the low-energy region, with the superimposed red dotted line showing the MDC maxima. (D,F) Low-energy MDC maxima and their linear fit corresponding to the bare and renormalized dispersions in the kink region for LSMO (D) and the LSMO|PZT (F) interface.

Finally, we will analyze the mechanism of FE-induced electron accumulation in terms of atomic orbitals. Fig. 4 A,B presents the ARPES images collected along the ΓM direction using s-polarized light. In principle, the dipole selection rules at our experimental geometry suggest

that these images reveal only the antisymmetric bands with the $e_g(x^2-y^2)$ character²¹. However, the low-temperature rhombohedral phase of LSMO lacks exact symmetry planes, and the mixture of domains with 3 different axis orientation^{26,30} relaxes this strict linear dichroism, surviving only at the Γ point, where the symmetry prevents $e_g(x^2-y^2)$ and $e_g(3z^2-r^2)$ bands from hybridization even under octahedral tilt and rotations³⁰. In Ref.⁸ it was shown that the FE instability propagating in LSMO alters the ideal overlap of the wavefunctions, their hopping probabilities and bandwidths, with the energy of e_g orbitals varying such that \mathbf{P} pointing towards LSMO interface lowers the $e_g(3z^2-r^2)$ energy and increases its occupation while opposite orientation of \mathbf{P} increases the $e_g(x^2-y^2)$ occupation. Assuming well-defined orbital character of the bands in the Γ point, the split of our e_g - derived bands, with the $e_g(x^2-y^2)$ - like band shifted towards E_F and consequent smaller k_F at the interface with PZT (Fig. 4B) compared to the bare LSMO (Fig. 4A) is consistent with the mechanism established before⁸. Hence the splitting $\Delta e_g = E[(3z^2-r^2)]-E[(x^2-y^2)]$, between the corresponding bands bottom relates to the different energy of the $e_g(3z^2-r^2)$ and $e_g(x^2-y^2)$ orbitals at our interfaces.³⁰ For the bare LSMO surface, the positive $\Delta e_g = 0.18 \text{ eV}$ is a direct indication of the higher energy and thus lower occupation of the $e_g(3z^2-r^2)$ orbital compared to the $e_g(x^2-y^2)$ one^{11,12}. At the interface with PZT, on the contrary, the negative $\Delta e_g = -0.2 \text{ eV}$ indicates the preferential occupation of the $3z^2-r^2$ orbital. The value $\Delta e_g = 0.15 \text{ eV}$ at the BTO|LSMO interface(Fig. S6) manifests an intermediate trend, with the relative $e_g(x^2-y^2)$ and $e_g(3z^2-r^2)$ energy only weakly modified by the smaller \mathbf{P} of BTO. On the theoretical side, our supercell DFT calculations confirm that such changes in the interfacial charge distribution depend on the magnitude of \mathbf{P} (Fig. 4F). The picture of the FE-dependent band filling of $e_g(3z^2-r^2)$ states (Fig. 4 C,D) is consistent with the trend established before in XAS measurements^{7,14} which identify different relative energies of LSMO e_g states triggered by the FE switch of the top layer (Fig. 4E).

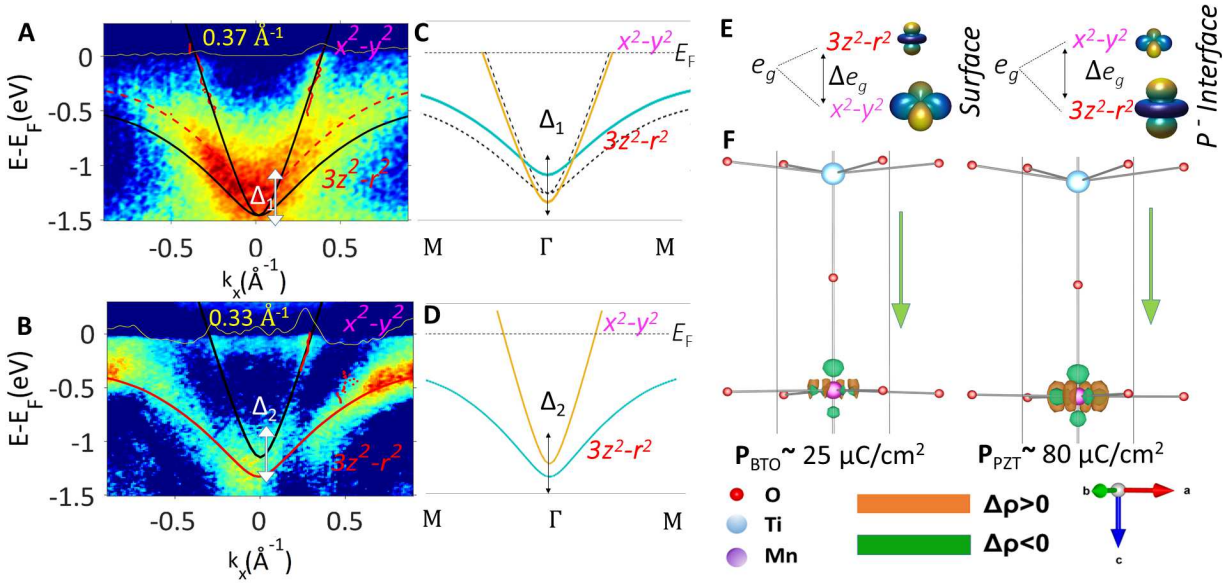


Figure 4. Orbital polarization. ARPES images along the ΓM direction measured at $h\nu=643$ eV and s -polarized light for (A) LSMO, and (B) LSMO|PZT interface. The MDC at E_F (yellow lines) are used to extract k_{FS} . The superimposed band calculations for strained LSMO are rigidly shifted for LSMO|PZT in order to match the experimental k_F . Δe_g in the Γ point measures energy splitting of the $(3z^2-r^2)$ - and (x^2-y^2) -derived bands. The sketch of the corresponding ARPES dispersions for bare LSMO assuming degenerate e_g orbitals (dotted line) and surface-lifted degeneracy (C) and LSMO|PZT interface (D) is based on the corresponding energies of the $(3z^2-r^2)$ - and (x^2-y^2) orbitals (E). (F) DFT slab calculations of the interface charge density for LSMO|BTO and LSMO|PZT shows how the modulation of charge carrier density in the first LSMO unit cell depends on the magnitude of the inwards P polarization.

Polaronic effective-mass renormalization. Quasi-2D hole polarons

We will now turn to the analysis of EPI manifested by renormalization of the charge carrier's m_{eff} . The ARPES images in Figure 2 A, B are overlaid by the MDC maxima, identifying the experimental band dispersions of bare LSMO (A) and PZT|LSMO interface (B). Closely following the theoretical band structure, upon approaching E_F , these dispersions go through a kink, which manifests as a renormalization of the bare bands and corresponding increase of m_{eff} . The kink position in the 40-70 meV range corresponds to the phonon modes active in thin LSMO layers^{25,31,32}, and indicates that it originates in the EPI. We stress that the observed kinks

are no artifacts due to energy or \mathbf{k} variations of the ARPES matrix element, but intrinsic properties of the $A(\mathbf{k},\omega)$ spectral function in LSMO as evidenced by qualitatively similar kink structures observed through higher BZs in k_{\parallel} as seen in Fig. 2 D-E, G-H and S3-S5.

Linear fits of the experimental dispersions in the bare-band and renormalized-band regions below and above the kink, respectively, yield the corresponding Fermi velocities and an estimate for the m_{eff} renormalization.

$$m_{\text{eff}}/m_b = v_F^b/v_F^* \quad (2)$$

Here, m_b and m_{eff} are the bare and renormalized effective masses, and v_F^b and v_F^* are bare and renormalized Fermi velocities, respectively.

The obtained m_{eff} values are compiled in Table 2. The enhancement of m_{eff} by a factor of ~ 3 for bare LSMO's hole band is consistent with the previous reports on epitaxially grown and substrate-strained LSMO from photoemission²⁷, optical conductivity³² and transport data³³. Intriguingly, the experimental m_{eff} dramatically decreases under the FE polarization in LSMO|PZT.

The mechanism of EPI in LSMO^{32,33} involves coupling of electrons with optical phonons through long-range Coulomb interaction as captured by the Fröhlich term³⁴:

$$|V_d(\mathbf{q})|^2 \sim \alpha/(q^{(d-1)} + \kappa^{(d-1)}) \quad (3)$$

where α is the dimensionless coupling constant, $d = 2$ or 3 the polaron dimensionality, \mathbf{q} the phonon wavevector, and κ the screening wavevector. Note that a d -dimensional polaron means that the electron is confined in d -dimensional space while the polarization is three-dimensional. This identifies the phonon-coupled charge carriers in the hole band as 2D polarons. For large Fröhlich polarons, the EPI strength is determined by the constant α . Except for extremely weak EPI, there is no analytic expression for α , and evaluation of the polaron properties requires unbiased exact numeric methods such as Feynman's path integral formalism³⁵ or Diagrammatic Monte Carlo (DMC)^{36,37}

Based on the experimental m_{eff} , we extracted the corresponding values of α^{2D} (Table 2) from DMC calculations for the 2D case³⁶ relevant for the hole bands. Whereas for bare LSMO the α^{2D} value lies in the intermediate-coupling regime of EPI, the FE polarization forces the Fröhlich polarons to transition to the weak-coupling regime. Eq. (3) shows that this can only be forced by the screening constant κ which increases with mobile charge density^{18,19}. However, the

experimental n_h in Table 1 shows the opposite trend, decreasing under the FE polarization at the LSMO|FE interface. Therefore the additional electrons building up in the interface region,⁴ play the decisive role in screening of the EPI and undressing the charge carriers from the phonons.

Due to insufficient statistics, the BTO|LSMO analysis of the hole band in terms of renormalized effective mass derived from the fit of the kink region is more challenging, hence we will formulate our conclusions on band renormalization based on the bare LSMO and PZT|LSMO data. However, the BTO|LSMO dataset is enough to establish the interface doping trend from the k_F variation (Table 1), which suggests a transition of the coupling strength to low coupling regime going from the LSMO surface to the P⁻ interface.

		LSMO	LSMO PZT
hole bands	m_{eff}/m_e	3.74 ± 0.42	1.69 ± 0.36
	α^{2D}	3.38	1.05
electron band	m_{eff}/m_e	2.50 ± 0.81	1.30 ± 0.4
	α^{3D}	4.07	1.5

Table 2 Mass renormalization and the EPI strength. Electron and hole m_{eff} deduced with Eq. (2) from the Fermi velocities obtained by a linear fit of the band dispersions in kink region. The dimensionless coupling constant $\alpha^{2D,3D}$, estimates the EPI strength for the 2D hole and 3D electron Frohlich polarons.

Polaronic effective-mass renormalization. 3D electron polarons

We will now return to the ARPES data for the $e_g(3z^2-r^2)$ derived electron bands in Fig. 3 for LSMO and the LSMO|PZT interface. Their dispersions in low-energy region, zoomed-in in (B,E), show the kink similar to the hole bands. Mapped by the MDC maxima in (C,F), the kink appears at approximately the same energy as in the hole bands, indicating its origin due to the EPI. Whereas for LSMO the kink and the corresponding renormalization of m_{eff} are distinct, for

its interface with PZT they are barely visible. From the linear fit of the band dispersions below and above the kink, we extracted the corresponding Fermi velocities of the bare and renormalized bands for LSMO and the LSMO|PZT interface, which yielded the m_{eff} -renormalization values compiled in Table 2. The kinks around other symmetry-related k_F points in Fig. 3 (A,B) show smaller spectral intensity, but yield essentially identical renormalization values. The corresponding coupling parameters α^{3D} , found from the DMC calculations in 3D case³⁷, are also given in Table 2. Similarly to the hole bands, the α^{3D} values exhibit a transition from the intermediate coupling regime in LSMO ($\alpha^{3D} \sim 4.1$) to weak coupling at the LSMO|PZT interface ($\alpha \sim 1.5$). This trend signals that the modulation of n_e due to the FE polarization provides better EPI screening. The same trend is identified for the bands dispersing along Γ M direction (Fig. S7 and SM 3.3). Although for BTO|LSMO we could not estimate α^{3D} with enough accuracy, the trend in n_e suggests an α^{3D} value intermediate between those of LSMO and PZT|LSMO.

The electrons attracted by the FE polarization into the interfacial region resolve the above puzzle why the depletion of the hole charge carriers goes along with the EPI reduction in the hole bands. Such effect has been observed in other manganites and is related to the fact that the electrons have much smaller m_{eff} compared to the holes. Being light, they are faster than the lattice oscillation and can therefore screen the EPI much more efficiently compared to the holes, whose m_{eff} in the third dimension is very large¹⁶. Hence, the light electrons are the carriers which set the interface to the weak-coupling regime of the Fröhlich polarons. Remarkably, the density of light electrons, n_e is smaller by more than one order of magnitude compared to that of the heavy holes n_h as seen in Table 1. However, the FE-induced increase of the light electron's n_e is enough to drive LSMO from the strong- to weak coupling regime. Moreover, the 3D character of interface electrons (Fig. 1H) suggests that the identified decrease of the polaronic coupling extends into the bulk beyond the Thomas-Fermi screening length¹⁷, implying the concomitant conductivity increase in a region exceeding the sharp interface region.

This is because the distribution of the 3D electrons, deriving from a complex interplay between interface potential and mutual dynamic screening, is not governed by the Thomas-Fermi theory. Hence the light electrons, with their 3D character, spread larger distances from the interface than the Thomas-Fermi length, providing static screening of slow lattice distortions even far from the interface.

Consequently, at the \mathbf{P}^+ interface we identify the expected electron accumulation and hole depletion. This translates in smaller adimensional polaronic coupling constant which indicates weaker electron-phonon interaction at the \mathbf{P}^+ .

This results shows that the light electron accumulation/depletion controlled by the FE state of the top material, by better/weaker screening the EPI is the key player in the modulated polaronic coupling at the FE/LSMO interface.

Outlook and perspectives

Our k-resolved soft X-ray photoemission results on multiferroic LSMO/BaTiO₃ and LSMO/PbZrTiO₃ heterostructures resolves (**A**) the missing ferroelectric, band-dependent electron/hole accumulation/depletion induced at the interface, extending the previous understanding of \mathbf{P} dependent modulation of orbital energies under FE switch^{7,8}.

Specifically, the FE instability propagating into the interfacial region of LSMO pushes the $e_g(x^2-y^2)$ derived bands defining the hole pockets around the R point, up in energy by ~0.2 eV, in accordance with the expected order of the LSMO e_g orbitals at the \mathbf{P}^+ interface^{7,8}. With the energy of the $(3z^2-r^2)$ orbitals, and their corresponding bands defining the electron pocket bands around the Γ point below the (x^2-y^2) ones, charge accumulation occurs in the former and charge depletion in the latter. This effect further propagates into (**B**) modulation of the EPI strength, expected changes in conductivity, allowing to tune the functionality of the interface. At relatively small influence of the heavy holes in the x^2-y^2 bands, the fast dynamic response of the light electrons in the $3z^2-r^2$ band effectively screens the EPI. Therefore, the electron accumulation in this band reduces the EPI strength from intermediate for bare LSMO to weak at its interface with the FE overlayer. This regime, with the charge excitations undressed from the lattice vibrations, increases the electron and hole itinerancy. The \mathbf{P}^+ FE polarization should therefore increase the charge carrier mobility, although this phenomenon still awaits verification in transport experiments, while the opposite FE state, by increasing the EPI strength, should decrease interface mobility. Such an effect of the FE polarization on the renormalization of m_{eff} through the EPI strength, which has escaped identification in the previous works, should be at play at

functional interfaces between the FE and oxide materials, adding at other existing mechanism of FE-assisted enhanced carrier mobility³⁸.

The detailed band-resolved picture disclosed by our results on how the **P** affects the orbital occupancy, band filling and electron-lattice interaction unveils a number of novel avenues towards further progress not only focused on the multiferroic oxide heterostructures discussed above, but also in the whole vast field of oxide electronics and spintronics. For example, **P** can be used to tune the mobility of the charge carriers in oxides through modified EPI, in turn modulated by the electron concentration. Particularly promising in this respect are systems where electron correlations increase the population of light-electron bands compared to heavy-hole ones similarly to Ce-doped CaMnO₃¹⁶. The electron correlations themselves can also be tuned through the band filling changing under the FE polarization (electron-correlation engineering). Furthermore, in multiband systems such as LSMO, where 2D charge carriers coexist with 3D ones, the polarization can tune their relative concentration and thus the dimensionality of the overall electron transport. Still to be explored is the oxide FE/superconductor heterostructures, where the polarization could be utilized to change the effective doping and the regime of phonon-mediated superconductivity³⁹ through the polarization-induced modulation of the EPI strength identified here for LSMO. Such mechanisms could be used, for example, for realization of switches for power-saving electronics based on Josephson junctions. These ideas open only a few of possible novel avenues towards realization of oxide electronic, spintronic, and superconducting devices based on our findings of the multifaceted effect of FE polarization on the orbital occupancy, band filling, electron correlations and electron-boson interaction.

Materials and Methods

Sample growth: Pulsed Laser Deposition

Epitaxial LSMO samples were grown on SrTiO₃ (STO) substrates using a thin (5 unit cells) SrRuO₃ (SRO) buffer layer between STO and LSMO. Heterostructures have been prepared by pulsed laser deposition using a well-established recipe to result in epitaxial growth as well as smooth surfaces and sharp interfaces^{3,9,23}.

The FE(3nm)/La_{0.7}Sr_{0.3}MnO₃(20nm)/SrRuO₃(2nm)/SrTiO₃ - (FE/LSMO/SRO/STO) and La_{0.7}Sr_{0.3}MnO₃(20nm)/SrRuO₃(2nm)/SrTiO₃ (LSMO/SRO/STO) samples were grown on (001) SrTiO₃ single crystals that were first cleaned in buffer solution of hydrofluoric acid (HF) and then annealed in air at 1000°C for 2 h. This treatment promotes an epitaxial growth of the films with atomic layer precision. The ablation of the FEs, SRO and LSMO targets was performed by using a KrF laser ($\lambda=248$ nm) and a repetition rate of 5Hz for SRO and FEs and 1Hz for LSMO. The laser fluence was 2J/cm² for the deposition of LSMO, SRO and PZT films, and 1.5J/cm² for BTO. The substrate temperature was maintained at 700°C and the oxygen pressure during deposition was 0.14 mbar for BTO and PZT, 0.13 mbar for SRO and 0.27mbar for LSMO. The as-grown LSMO, SRO and BTO films were post-deposition annealed, in the deposition chamber, at 700°C, for one hour, in O₂ atmosphere while post-annealing of PZT was performed at 575°C to prevent Pb migration. Then, they were transferred in N₂ atmosphere from the preparation chamber to the analysis one, which we notice to bring only a minimum surface contamination easy to overcome by the high probing depth of the soft X-ray range.

SX-ARPES

Experiments were carried out at ADRESS beamline at Swiss Light Source which delivers high photon flux in soft X-ray range²¹, allowing the band structure investigation of buried interface with the additional benefit of a remarkably sharp momentum resolution along the out-of-plane direction k_z ²⁰ and thus full 3D momentum. The relationship between electron momentum (k_{\parallel}, k_{\perp}), photoelectron kinetic energy and the photoelectron emission angle are given in Ref. ²¹. The geometry of the experimental setup²¹ is such that the incoming s-polarized

(p-polarized) photon beam has the electric field oscillating perpendicularly (parallel) to the measurement plane, thus the selection rules of the photoemission process permit to probe only the antisymmetric (symmetric) states with respect to that measurement plane. ARPES measurements have been performed in pressure better than 10-10 mbar and a temperature of 12 K. Fermi level is calibrated using a gold foil in electrical contact with the sample. A combined resolution (thermal broadening in addition to the photon beam and the ARPES analyzer) was \sim 70 meV.

Transmission electron microscopy (TEM)

Transmission electron microscopy observations have been performed using a probe-corrected analytical high-resolution JEM ARM 200F electron microscope operated at 200 kV, equipped with a Gatan Quantum SE Image Filter for EELS. Atomic resolution images have been recorded in STEM mode (0.08 nm point resolution) using the High-Angle Annular Dark Field (HAADF) detector. Chemical maps at atomic resolution have been obtained by EELS-SI in the STEM mode. Images and spectral data processing have been made using specialized routines under Gatan Digital Micrograph. For the atomic-resolution spectrum-image experiments the electron beam has been scanned inside a 25 nm² across the interface region. The probe dwell time was set at 20 ms/pixel. The chosen convergence angle was 2.6 mrad using a condenser aperture of 30 μ m diameter, while the collection angle was 18 mrad at 3 cm camera length and for the spectrometer entrance aperture of 2.5 mm. The energy dispersion and the spectral window were set in such a way to allow the simultaneous acquisition of the Ti L, O K, Mn L, Ba L and La M signals.

First-principles calculations

The calculations were performed within the generalized gradient approximation (GGA) using the quantum ESPRESSO plane-wave code^{40,41}, and the exchange-correlation functional in the Perdew–Burke–Ernzerhof (PBE) parametrization. We used norm-conserving pseudopotentials from PseudoDojo⁴². The heterostructure was modeled by a 1×1×14 supercell geometry starting from the relaxed structure of the LSMO unit cell, but imposing the calculated in-plane lattice constant $a=3.903$ Å of SrTiO₃. This supercell contained 7 unit cells (u.c.) of BTO and PTO in

contact with 7 u.c. of LSMO. This thickness ensures that the FE property remains stable, because the FE-polarization states tend to merge starting from a thickness of 5 u.c.⁴³. The z-coordinates were allowed to relax until the Hellman-Feynman forces on each atom were less than 2.5 meV/Å. La-Sr substitutional doping was treated by means of virtual crystal approximation (VCA) replacing each A-site of the perovskite with a fictitious atom with fractional valence, instead of explicit doping which would be computationally expensive due to larger supercells.

The kinetic-energy cut-off for the plane waves was set at 60 Ry and for the charge density at 240 Ry. The BZ integration was performed on an automatically generated Monkhorst-Pack $3 \times 3 \times 3$ k-mesh, for all slabs, with Gaussian energy-level smearing of 0.02 Ry. For bulk LSMO band structure, a $U_{Mn}=2\text{eV}$ Hubbard parameter was employed, which reproduces well the half-metallic character of the LSMO.

Data availability

All data presented in this work are available from the corresponding authors upon request.

Acknowledgments

This work was funded by the Romanian UEFISCDI Agency under Contract No. PN-III-P4-ID-PCCF2016-0047. D.G.P aknowledges funding from PN-II-RU-TE 150/2015 project. M.-A.H. acknowledges the support of the Swiss Excellence Scholarship grant ESKAS-no. 2015.0257 and of the Romanian UEFISCDI Agency under Contract No. PN-III-P4-ID-PCE-2020-2540. SX-ARPES measurements were performed at the ADRESS beamline from Swiss Light Source under the proposals no. 20151375, 20160516 and 20170810. ASM acknowledge JST CREST Grant Number JPMJCR1874, Japan. F.B. acknowledges funding from Swiss National Science Foundation under Grant Agreement No. 200021_146890 and from

European Community's Seventh Framework Programme (FP7/2007-2013) under Grant Agreement No. 290605 (PSIFELLOW/COFUND)

Author Contributions

MAH elaborated the idea of the experiments with assistance from VNS and LP. LEH prepared the samples assisted by of LP. MAH, DGP, FB, LLL performed the SX-ARPES measurements assisted by VNS and TS, IP performed XRD analyses, RN and CI performed TEM investigations, MAH and LDF performed ab-initio calculations. ASM provided the picture of coexisting 2D and 3D polarons. MAH, DGP and FB processed the photoemission data assisted by VNS and CMT. MAH and VNS wrote the manuscript with input from all the authors.

Competing Interest Statement:

There are no competing interests

References

1. Molegraaf, H. J. A. *et al.* Magnetoelectric Effects in Complex Oxides with Competing Ground States. *Advanced Materials* vol. 21 3470–3474 (2009).
2. Vaz, C. A. F. *et al.* Origin of the magnetoelectric coupling effect in Pb (Zr 0.2 Ti 0.8) O 3/La 0.8 Sr 0.2 MnO 3 multiferroic heterostructures. *Phys. Rev. Lett.* **104**, 127202 (2010).
3. Pintilie, I. *et al.* Polarization-Control of the Potential Barrier at the Electrode Interfaces in Epitaxial Ferroelectric Thin Films. *ACS Applied Materials & Interfaces* vol. 6 2929–2939 (2014).
4. Popescu, D. G., Barrett, N., Chirila, C., Pasuk, I. & Husanu, M. A. Influence of hole

- depletion and depolarizing field on the BaTiO₃/La_{0.6}Sr_{0.4}MnO₃ interface electronic structure revealed by photoelectron spectroscopy and first-principles calculations. *Physical Review B* vol. 92, 235442 (2015).
5. Peters, J. J. P., Apachitei, G., Beanland, R., Alexe, M. & Sanchez, A. M. Polarization curling and flux closures in multiferroic tunnel junctions. *Nature Communications* vol. 7, 13484 (2016).
 6. Pruneda, J. M. *et al.* Ferrodistortive Instability at the (001) Surface of Half-Metallic Manganites. *Physical Review Letters* vol. 99, 226101 (2007).
 7. Preziosi, D., Alexe, M., Hesse, D. & Salluzzo, M. Electric-Field Control of the Orbital Occupancy and Magnetic Moment of a Transition-Metal Oxide. *Physical Review Letters* vol. 115, 157401 (2015).
 8. Chen, H. *et al.* Reversible Modulation of Orbital Occupations via an Interface-Induced Polar State in Metallic Manganites. *Nano Letters* vol. 14 4965–4970 (2014).
 9. Tănase, L. C. *et al.* Polarization Orientation in Lead Zirconate Titanate (001) Thin Films Driven by the Interface with the Substrate. *Physical Review Applied* vol. 10, 034020 (2018).
 10. Rault, J. E. *et al.* Interface electronic structure in a metal/ferroelectric heterostructure under applied bias. *Physical Review B* vol. 87 (2013).
 11. Tebano, A. *et al.* Evidence of Orbital Reconstruction at Interfaces in Ultrathin La_{0.67}Sr_{0.33}MnO₃ Films. *Physical Review Letters* vol. 100 (2008).
 12. Pesquera, D. *et al.* Surface symmetry-breaking and strain effects on orbital occupancy in transition metal perovskite epitaxial films. *Nature Communications* vol. 3 (2012).
 13. Moon, E. J. *et al.* Effect of Interfacial Octahedral Behavior in Ultrathin Manganite Films. *Nano Letters* vol. 14 2509–2514 (2014).

14. Cui, B. *et al.* Manipulation of Electric Field Effect by Orbital Switch. *Advanced Functional Materials* vol. 26 753–759 (2016).
15. Bardeen, J., Cooper, L. N. & Schrieffer, J. R. Theory of Superconductivity. *Physical Review* vol. 108 1175–1204 (1957).
16. M.-A. Husanu, L. Vistoli, C. Verdi, A. Sander, V. Garcia, J. Rault, F. Bisti, L. L. Lev, T. Schmitt, F. Giustino, A. S. Mishchenko, M. Bibes & V. N. Strocov. Electron-polaron dichotomy of charge carriers in perovskite oxides. *Communications Physics* **3**, 62 (2020).
17. Yamada, H. *et al.* Ferroelectric control of a Mott insulator. *Sci. Rep.* **3**, 2834 (2013).
18. Cancellieri, C. *et al.* Polaronic metal state at the LaAlO₃/SrTiO₃ interface. *Nature Communications* vol. 7 (2016).
19. Verdi, C., Caruso, F. & Giustino, F. Origin of the crossover from polarons to Fermi liquids in transition metal oxides. *Nature Communications* vol. 8 (2017).
20. Strocov, V. N. Intrinsic accuracy in 3-dimensional photoemission band mapping. *Journal of Electron Spectroscopy and Related Phenomena* vol. 130 65–78 (2003).
21. Strocov, V. N. *et al.* Soft-X-ray ARPES facility at the ADRESS beamline of the SLS: concepts, technical realisation and scientific applications. *Journal of Synchrotron Radiation* vol. 21 32–44 (2014).
22. Shin, Y. J. *et al.* Interface Control of Ferroelectricity in an SrRuO₃ /BaTiO₃ /SrRuO₃ Capacitor and its Critical Thickness. *Advanced Materials* vol. 29 1602795 (2017).
23. Pintilie, L. *et al.* Polarization induced self-doping in epitaxial Pb(Zr_{0.20}Ti_{0.80})O₃ thin films. *Scientific Reports* vol. 5 (2015).
24. Teodorescu, C. M. Ferroelectricity in thin films driven by charges accumulated at interfaces. *Phys. Chem. Chem. Phys.* **23**, 4085–4093 (2021).

25. Merten, S., Bruchmann-Bamberg, V., Damaschke, B., Samwer, K. & Moshnyaga, V. Jahn-Teller reconstructed surface of the doped manganites shown by means of surface-enhanced Raman spectroscopy. *Physical Review Materials* vol. 3 (2019).
26. Lev, L. L. *et al.* Fermi Surface of Three-Dimensional $\text{La}_{1-x}\text{Sr}_x\text{MnO}_3$ Explored by Soft-X-Ray ARPES: Rhombohedral Lattice Distortion and its Effect on Magnetoresistance. *Physical Review Letters* vol. 114 (2015).
27. Horiba, K. *et al.* Isotropic Kink and Quasiparticle Excitations in the Three-Dimensional Perovskite Manganite $\text{La}_{0.6}\text{Sr}_{0.4}\text{MnO}_3$. *Physical Review Letters* vol. 116 (2016).
28. Luttinger, J. M. Fermi Surface and Some Simple Equilibrium Properties of a System of Interacting Fermions. *Physical Review* vol. 119 1153–1163 (1960).
29. Jia, C.-L. *et al.* Direct Observation of Continuous Electric Dipole Rotation in Flux-Closure Domains in Ferroelectric $\text{Pb}(\text{Zr},\text{Ti})\text{O}_3$. *Science* vol. 331 1420–1423 (2011).
30. Matt, C. E. *et al.* Direct observation of orbital hybridisation in a cuprate superconductor. *Nat. Commun.* **9**, 972 (2018).
31. Björnsson, P. *et al.* Lattice and charge excitations in $\text{La}_{1-x}\text{Sr}_x\text{MnO}_3$. *Physical Review B* vol. 61 1193–1197 (2000).
32. Hartinger, C., Mayr, F., Loidl, A. & Kopp, T. Polaronic excitations in colossal magnetoresistance manganite films. *Physical Review B* vol. 73 (2006).
33. Asamitsu, A. & Tokura, Y. Hall effect in $\text{La}_{1-x}\text{Sr}_x\text{MnO}_3$. *Physical Review B* vol. 58 47–50 (1998).
34. Fröhlich, H. Electrons in lattice fields. *Adv. Phys.* **3**, 325–361 (1954).
35. Rosenfelder, R. & Schreiber, A. W. On the best quadratic approximation in Feynman's path integral treatment of the polaron. *Phys. Lett. A* **284**, 63–71 (2001).

36. Hahn, T., Klimin, S., Tempere, J., Devreese, J. T. & Franchini, C. Diagrammatic Monte Carlo study of Fröhlich polaron dispersion in two and three dimensions. *Physical Review B* vol. 97 (2018).
37. Mishchenko, A. S., Prokof'ev, N. V. & Sakamoto, A. Diagrammatic quantum Monte Carlo study of the Fröhlich polaron. *Phys. Rev. B: Condens. Matter Mater. Phys.* (2000).
38. Sluka, T., Tagantsev, A. K., Bednyakov, P. & Setter, N. Free-electron gas at charged domain walls in insulating BaTiO₃. *Nat. Commun.* **4**, 1808 (2013).
39. Grimaldi, C., Pietronero, L. & Strässler, S. Nonadiabatic Superconductivity: Electron-Phonon Interaction Beyond Migdal's Theorem. *Physical Review Letters* vol. 75 1158–1161 (1995).
40. Giannozzi, P. *et al.* Advanced capabilities for materials modelling with Quantum ESPRESSO. *J. Phys. Condens. Matter* **29**, 465901 (2017).
41. Giannozzi, P. *et al.* QUANTUM ESPRESSO: a modular and open-source software project for quantum simulations of materials. *J. Phys. Condens. Matter* **21**, 395502 (2009).
42. van Setten, M. J. *et al.* The PseudoDojo: Training and grading a 85 element optimized norm-conserving pseudopotential table. *Comput. Phys. Commun.* **226**, 39–54 (2018).
43. Dorin, R., Filip, L. D., Pintilie, L., Butler, K. T. & Plugaru, N. Designing functional ferroelectric interfaces from first-principles: dipoles and band bending at oxide heterojunctions. *New J. Phys.* **21**, 113005 (2019).
44. Cui, B. *et al.* Magnetoelectric Coupling Induced by Interfacial Orbital Reconstruction. *Adv. Mater.* **27**, 6651–6656 (2015).
45. Yu, P. *et al.* Interface control of bulk ferroelectric polarization. *Proc. Natl. Acad. Sci. U. S. A.* **109**, 9710–9715 (2012).

46. Spurgeon, S. R. *et al.* Polarization screening-induced magnetic phase gradients at complex oxide interfaces. *Nat. Commun.* **6**, 6735 (2015).
47. Chikina, A. *et al.* Orbital Ordering of the Mobile and Localized Electrons at Oxygen-Deficient LaAlO₃/SrTiO₃ Interfaces. *ACS Nano* **12**, 7927–7935 (2018).

Supplementary Material

Ferroelectricity modulates polaronic coupling at multiferroic interfaces

Marius Adrian Husanu^{1,2}, Dana Georgeta Popescu², Federico Bisti^{1,3}, Luminita Mirela Hrib², Lucian Dragos Filip², Iuliana Pasuk², Raluca Negrea², Cosmin Istrate², Leonid Lev⁴, Thorsten Schmitt¹, Lucian Pintilie², Andrey Mishchenko⁵, Cristian Mihail Teodorescu² and Vladimir N. Strocov¹⁺*

1. X-ray photoelectron spectroscopy measurements

The compensation of the FE polarization and screening of the localized depolarizing charges by mobile electrons and holes close to the FE/vacuum interface manifest in downwards or upwards band bending, and further reflects in rigid shifts of all core levels towards lower (\mathbf{P}^-) or higher (\mathbf{P}^+) binding energies.

In our case, the \mathbf{P}^- state of the ferroelectric is in accordance with previous observations when LSMO was used as a substrate^{4,5,44–46}. Our established FE state comes from following the FE-dependent shift of the core levels, related to the evolution of the band bending potential going from the surface of the ferroelectric towards the interface. Fig S1A shows the shift towards higher energies of Ti $2p$ level in BTO when we gradually increase the probing depth (Fig. S1B) confirming the variation of the band bending potential as expected for its \mathbf{P}^- state. The PZT layer lying in the same FE state as BTO is confirmed by comparing the Ti $2p$ and Pb $4f$ core level energies (Fig. S1 C,D) with the corresponding ones when PZT is deposited on Nb-doped STO, which is known to feature \mathbf{P}^+ FE state⁹. The relative shift of 0.9 eV towards lower binding energies of both Pb and Ti core levels is consistent with the values corresponding to opposed FE state.

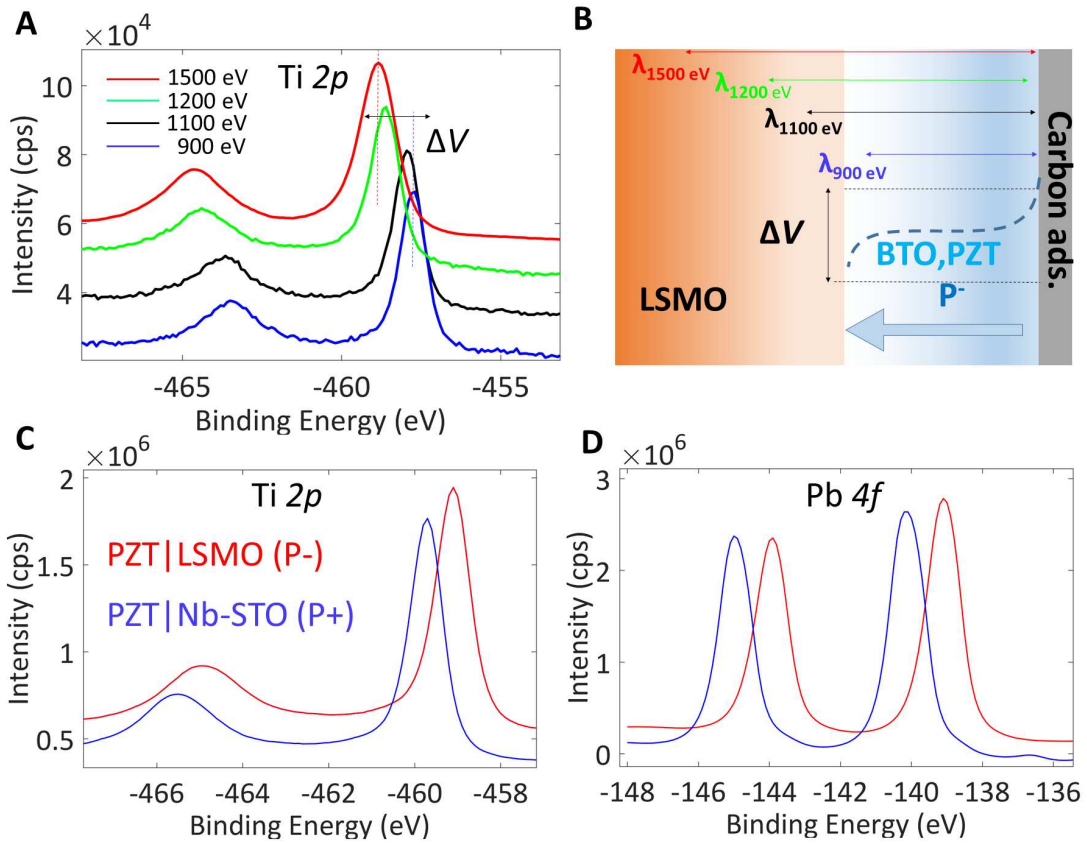


Figure S1 FE character from binding energy shifts. (A) Variation of Ti 2p core level as a function of the energy-dependent probing depth (B) Sketch of the band bending close to the surface of the FE with the FE polarization pointing towards the sample (\mathbf{P}^-) at the interface with the vacuum and the accompanying bending of electronic bands upwards in a model of rigid shifts of the core levels towards lower binding energies. Ti 2p (C) and Pb 4f (D) XPS spectra recorded on 5 nm PZT deposited on LSMO/Nb:STO (\mathbf{P}^+) and LSMO/SRO/STO (\mathbf{P}^-)

2. Crystaline structure, epitaxial growth and compressive strain

The overall atomic level smoothness of the interfaces and the high crystalline quality of the LSMO film is evidenced by the occurrence of Pendellosung fringes accompanying the Bragg maxima of the film. The fringes are better resolved for LSMO grown on SRO, than for LSMO grown directly on STO (inset of Fig. S2 C). The reciprocal space mapping (RSM) image

recorded around the peak of the STO substrate (Fig. S2 D and E) reveal the fully strained in-plane structure of LSMO ($a_{LSMO} = a_{STO} = 3.905 \text{ \AA}$). The out-of-plane lattice parameter determined from the 2θ - ω scan is 3.856 \AA . Therefore, compared to the pseudocubic bulk LSMO ($a=3.87 \text{ \AA}$), the film structure is in-plane tensile strained to fit the substrate lattice, leading to a compressive perpendicular strain.

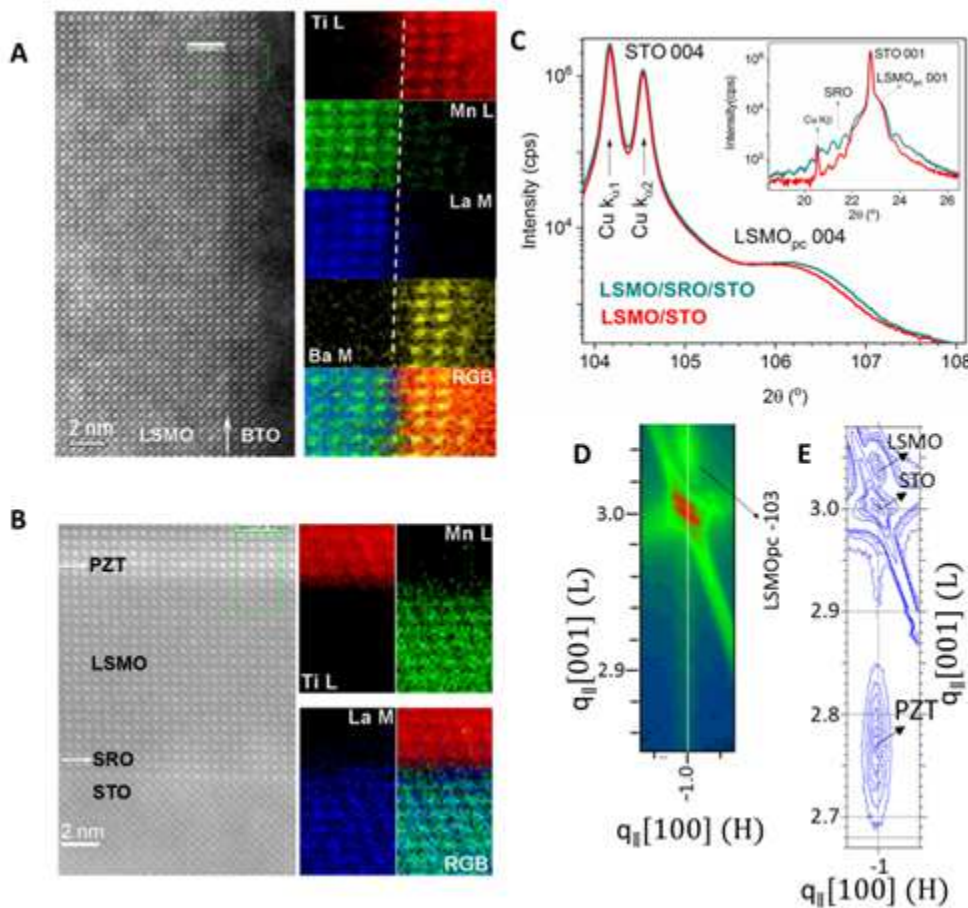


Figure S2 Crystalline structure High resolution HAADF – STEM images of FE/LSMO heterostructure showing the morphology of the deposited layers and the BTO/LSMO (**A**) and PZT/LSMO interfaces (**B**). 2θ - ω scans zoomed around STO (004) used for determining the out-of-plane lattice constant of LSMO and around STO (001) (inset) revealing the Pendellösung fringes (**C**); The Reciprocal Space Mapping of the heterostructure around (-103) peak of STO for BTO|LSMO (**D**) and PZT|LSMO (**E**). The subscript pc refers to pseudo-cubic indexing.

3. ARPES data:

Isoenergetic scans in k_z direction (Figure 1D), performed by varying the incoming energy from 480 eV to 750 eV while keeping the k_{\parallel} in the X_yMR and in $\Gamma X_xM'$ planes, reveal respectively the heavy-hole cuboids and light-electron spheres structure of the interface \mathbf{k} space, in accordance with our calculated Fermi surface. The 643 eV energy brings the electron states close to the Γ point in k_z for k_{\parallel} in the second Brillouin zone, while the hole bands are ideally probed with the 708 eV energy (Fig. 1E,F). The 643 eV radiation, in resonance with Mn 2p - Mn 3d intra-atomic transition, selectively enhance the Mn³⁺/Mn⁴⁺ interface states, thus allowing their identification at a better signal-to-noise ratio^{18,20,26,47}.

3.1 Hole bands in extended k-space and fit of the momentum distribution curves

The electron dynamics as the result of electron interaction with other quasiparticles can be described by the Green function:

$$G(E, k) = \frac{1}{E - \varepsilon(k) - \Sigma(k, \omega)} \quad (\text{S1})$$

related to the spectral function, which is the essential result in ARPES by:

$$A(E, k) = -\frac{1}{\pi} \text{Im}[G(E, k)] = -\frac{1}{\pi} \frac{\Sigma''(\omega)}{[E - \varepsilon(k) - \Sigma'(\omega)]^2 + [\Sigma''(\omega)]^2} \quad (\text{S2})$$

In Eq. S3, ε is the bare band dispersion and Σ is the complex self energy which captures effects going beyond the single particle picture. The non-interacting case is described by .

The real part of the self energy captures the effect of energy renormalization as the result of interactions and corresponds to the difference between the parabolic bare band dispersion, and renormalized one extracted from the MDC maxima. The imaginary part is related to the finite lifetime of the excited states and depends on the correlated nature of the system and/or scattering with impurities.

MDCs were obtained by integrating the corrected raw data in a 0.01 eV energy window. Correction of data involves extracting an incoherent, angle integrated contribution from the raw data. The MDC maxima were extracted from Lorenzian fit of MDCs, $\pm 0.15 \text{ \AA}^{-1}$ around each $k_F^{-1,0,1}$ (Figs. S 3A-S 5A) and 2nd order polynomial to account for the smooth varying background.

Bare and renormalized Fermi velocities were then derived as the slopes of the linear fits for the MDC maxima-derived bare and kink-renormalized regions in the band structure (Supplementary Table1). Their ratio gives the renormalization of the m_{eff} as a result of the electrons dressed with the elementary excitations, phonons in our case.

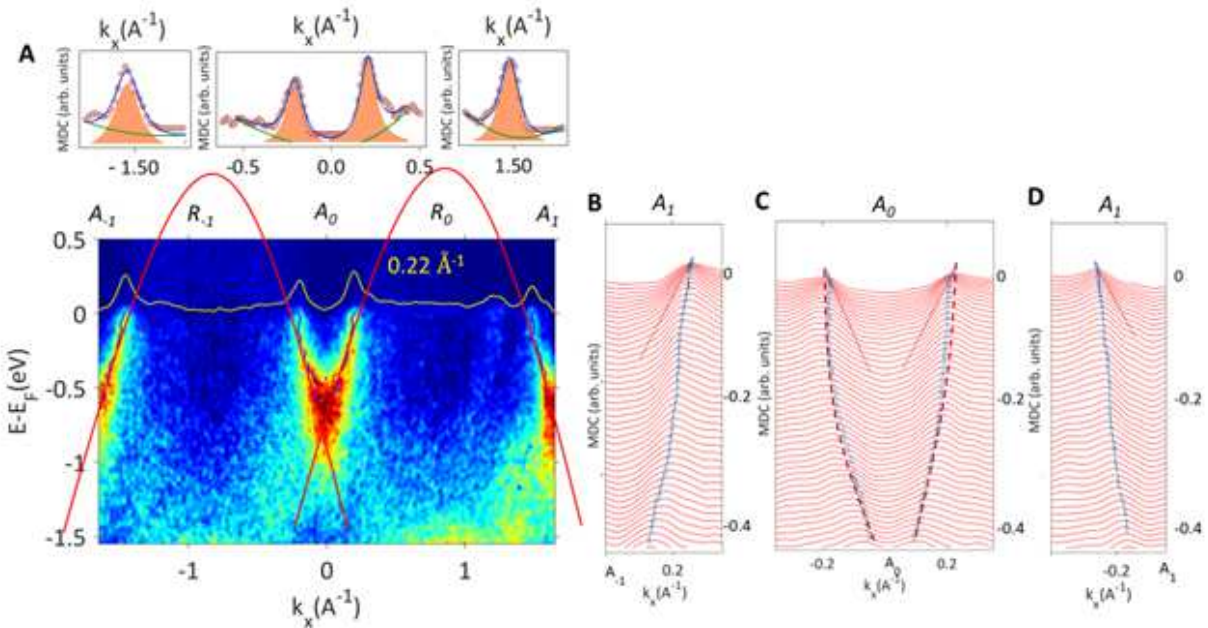


Fig. S3 ARPES image recorded with $h\nu=708$ eV through the hole cuboids at the LSMO surface (A) ARPES map recorded through the hole cuboids at the LSMO surface and the accompanying Lorenzian fit $\pm 0.15 \text{ \AA}^{-1}$ of the MDC at the Fermi energy around all $A_{-1,0,1}$ points . The same fit algorithm has been used to fit all MDCs down to -0.4 eV. The red lines are visual guides of the detected hole bands. The kinks in the band structure are evident in all $A_{-1,0,1}$ points through deviations of the Fermi velocity v_F^* from that of the bare band v_F (B, C, D).

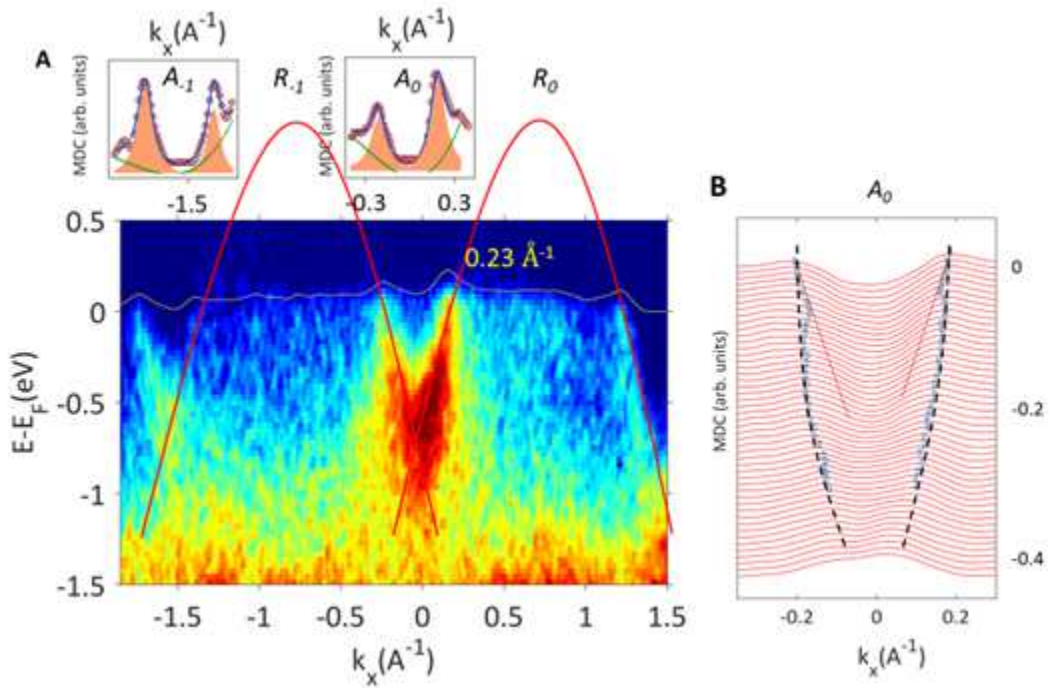


Figure S4 ARPES image recorded with $h\nu=708$ eV through the hole cuboids at the LSMO/BTO interface. (A) ARPES map through the hole cuboids at the LSMO/BTO interface and the accompanying Lorenzian fit $\pm 0.15 \text{ \AA}^{-1}$ of the MDC at the Fermi energy around all $A_{-1,0}$ points. The same fit algorithm has been used to fit all MDCs down to -0.4 eV.. The red lines are visual guides of the detected hole bands. The kinks in the band structure are evident in A_0 point through deviations of the Fermi velocity v^*_F from that of the bare band v_F (C,D).

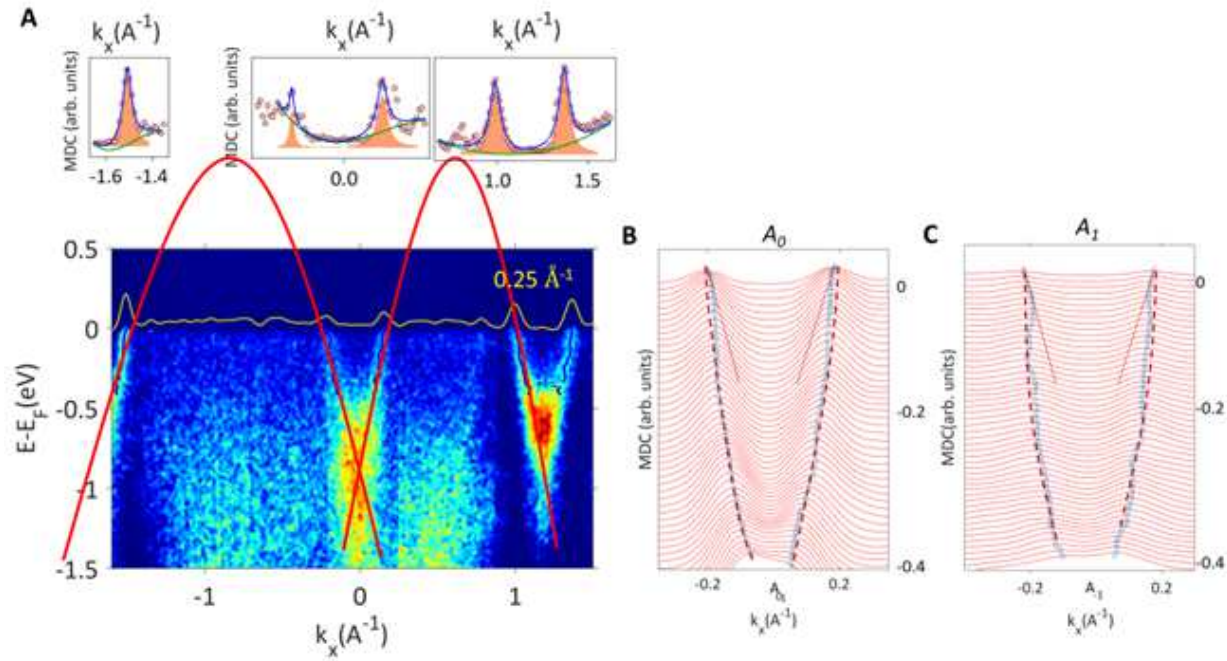


Figure S5 ARPES image recorded with $h\nu=708$ eV through the hole cuboids at the LSMO|PZT interface (A) ARPES map through the hole cuboids at the LSMO|PZT interface and the accompanying Lorenzian fit $\pm 0.15 \text{\AA}^{-1}$ of the MDC at the Fermi energy around all $A_{-1,0,1}$ points . The same fit algorithm has been used to fit all MDCs down to -0.4 eV. The red lines are visual guides of the detected hole bands. The kinks in the band structure are evident in all $A_{-1,0,1}$ points through deviations of the Fermi velocity v_F^* from that of the bare band v_F (**C,D**).

3.2 Electron bands for LSMO/BTO interface

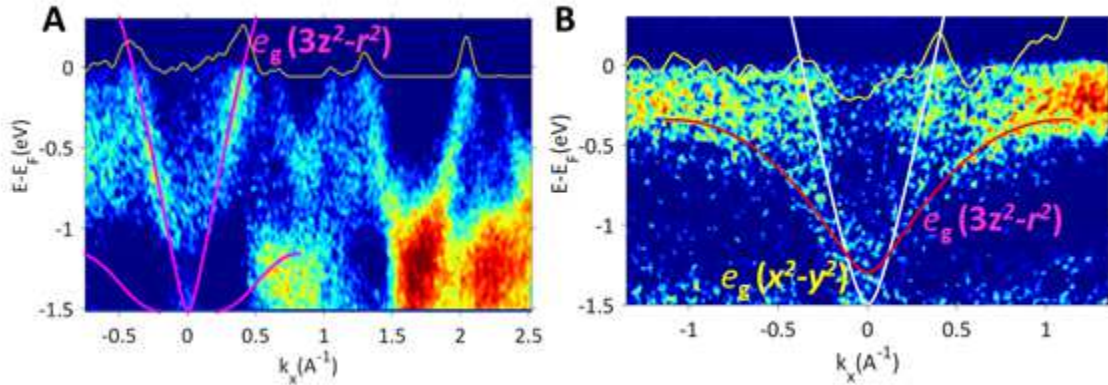


Figure S6 ARPES images on LSMO|BTO multiferroic interface along Γ X (**A**) and Γ M (**B**) directions recorded with $h\nu=643$ eV

By separately matching the calculated band structure at the experimental \mathbf{k}_F of the $e_g(x^2-y^2)$ and experimental dispersion of the $e_g(3z^2-r^2)$ band, we estimate the density of carriers embedded in $e_g(x^2-y^2)$ band (Supplementary Table 1) and determine the splitting between the two bands, $\Delta e_g = 0.15$ eV associated with the lifting of the degeneracy at the LSMO/BTO interface under combined effect of substrate-strain, termination and FE polarization pointing towards LSMO.

3.3 Mass renormalization along the Γ M direction

Electrons along Γ M	LSMO surface	LSMO BTO	LSMO PZT
k_F (\AA^{-1})	0.37 ± 0.08	0.36 ± 0.10	0.33 ± 0.09
n (cm^{-3})	0.86×10^{21}	0.79×10^{21}	0.61×10^{21}

Supplementary Table 1 Experimental Fermi wavevectors extracted from MDCs at the Fermi energy for the bands defining the electron pockets in the Γ point along the Γ M direction and their estimated carrier densities

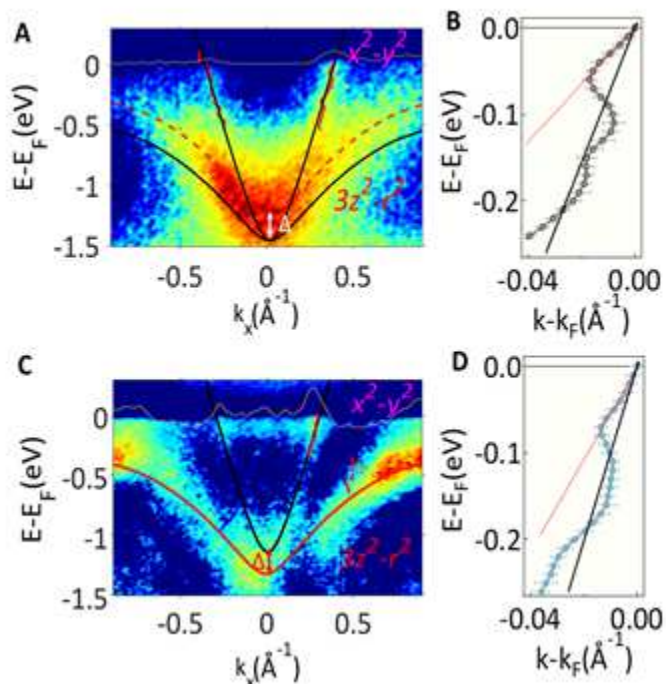


Figure S7. Mass renormalization along the Γ M direction. ARPES images recorded along Γ M direction, probing the electron-derived bands with 643 eV energy and s-polarized light for bare

LSMO surface (**A**) and LSMO|PZT (**C**) interface. Red dots superimposed on each image are the MDC maxima with MDC at E_F (yellow lines) used to extract k_F s. Calculated band structure for strained LSMO is rigidly shifted in order to match the experimental k_F . The splitting of $(3z^2-r^2)$ and (x^2-y^2) - derived bands, Δe_g , is direct indication of separation in the Γ point of the two bands with different orbital character. Linear fit of MDC maxima in the low energy range used to extract the Fermi velocities for LSMO surface (**B**) and PZT|LSMO (**D**).

	LSMO surface	LSMO PZT
	Γ M	Γ M
v_F^b	9.10 ± 0.41	9.10 ± 0.35

v_F^*	3.33±0.14	5.32±0.38
m_{eff}/m	2.73±0.55	1.71±0.73
α	4.31	2.86

Supplementary Table 2 Fermi velocities for the bare band (v_F^b), the renormalized value (v_F^*) in the region close to the Fermi energy, featuring the kink in the band dispersions along the ΓM direction and the adimensional constant α , measuring the EPI strength for the carriers in the (x^2-y^2) -derived electron band

Supplementary Methods

XRD measurements

The lattice parameters of the epitaxial structures have been determined by high resolution X-ray diffraction, using a Bruker D8 Advance X-ray diffractometer with nickel-filtered Cu K α radiation, parallelized with a Göbel mirror. Symmetric scans with miscut correction ($2\theta-\omega$ scans) were performed to evaluate the structural characteristics perpendicular to the substrate. Reciprocal-space mappings (RSM) around the STO node were performed to confirm the epitaxy on the whole area and thickness of the thin layers, and to estimate the in-plane lattice parameters and the epitaxial strain. The lattice parameters of the thin films were determined using the reflections of the cubic STO substrate ($a=3.905 \text{ \AA}$) as the reference.

